RSC Advances

PAPER

View Article Online
View Journal | View Issue

Cite this: *RSC Adv.*, 2020, **10**, 29402

Ultrafine Pd nanoparticles loaded benzothiazole-linked covalent organic framework for efficient photocatalytic C–C cross-coupling reactions†

Yongliang Yang,[ab] Hongyun Niu,[a] Weijia Zhao,[ab] Lin Xu,[a] Hui Zhang[a] and Yaqi Cai*[acd]

Received 26th April 2020
Accepted 3rd August 2020

DOI: 10.1039/d0ra03739g

rsc.li/rsc-advances

We proposed a strategy that a benzothiazole-linked covalent organic framework (**TTT-COF**) was used as a substrate to prepare metal composite photocatalyst **Pd NPs@TTT-COF**. Firstly, benzothiazole linked **TTT-COF** exhibited superior chemical stability and photoresponse. Moreover, a finer particle size (2.01 nm) and more uniform distribution of Pd NPs were observed in **Pd NPs@TTT-COF** owing to the binding interaction between Pd NPs and S in benzothiazole groups. **Pd NPs@TTT-COF** exhibited superior efficiency and reusability in photocatalytic C–C cross-coupling reactions. Mechanism study suggested that photogenerated electrons and holes on **TTT-COF** played important roles in these reactions.

Introduction

Covalent Organic Frameworks (COFs) are a class of conjugated porous organic materials constructed with organic building units *via* strong covalent bonds.[1–3] To date, most research on the design of COFs has been focused on regulating the chemical structure of the organic modules. It's worth noting that the linkage of COFs is also crucial to the properties of COFs. Dynamic covalent linkages between building blocks are necessary for the construction of crystalline and ordered COFs architectures, but are not conducive to the robustness of COFs,[2] which is a major impediment to the applications. Recently, the exploration of novel linkages has become the focus in the development of COFs, a series of novel covalent linkages such as olefin linkage,[4] benzimidazole[5]/benzoxazole[6]/benzothiazole[7] linkages, amide linkage,[8] dioxin linkage[9] have been reported, which could not only enhance the chemical stability compared to the COFs based on boronate ester linkage and imine linkage, adopted by a majority of known COFs, but also exhibited more fascinating and unique properties.

Metal nanopaticles (NPs) are widely used as heterogeneous catalysts in chemical synthesis due to their high surface area and ultrafine size distribution. However, the ultrafine metal clusters tend to gradually accumulate on account of their high surface energy and result in the deactivation of the catalysts.[10] Therefore, stable and uniform supporting substrates are necessary for metal NPs catalysts, and COFs are suitable for being adopted as a kind of substrates. On the one hand, on the basis of regular and tunable pore structure as well as high surface area of COFs, ultrafine metal clusters can be embedded on the pores of COFs with confined nano sizes uniformly. On the other hand, heteroatoms can be artificially introduced into the COFs frameworks owing to the designability of COFs building blocks, thus metal clusters can be anchored in the pores *via* the binding interactions between metal atoms and heteroatoms. Zhang's group has reported some metal NPs-COFs hybrid materials as stable and efficient heterogeneous catalysts,[11,12] whose COFs substrates were synthesized from the precursors containing heteroatoms (S, P).

Here in, we propose an ingenious strategy to load Pd NPs on photoactive benzothiazole-linked **TTT-COF** as a Mott–Schottky

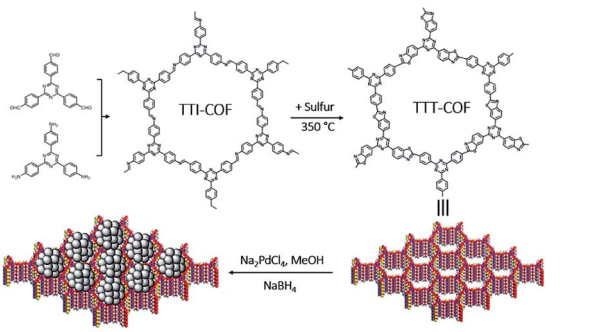

Scheme 1 Graphical representation of the synthesis of **Pd NPs@TTT-COF**.

[a]*State Key Laboratory of Environmental Chemistry and Ecotoxicology, Research Center for Eco-Environmental Sciences, Chinese Academy of Sciences, Beijing, 100085, China. E-mail: caiyaqi@rcees.ac.cn*

[b]*University of Chinese Academy of Sciences, Beijing 100049, China*

[c]*Institute of Environment and Health, Jianghan University, Wuhan 430056, China*

[d]*Institute of Environment and Health, Hangzhou Institute For Advanced Study, UCAS, China*

† Electronic supplementary information (ESI) available. See DOI: 10.1039/d0ra03739g

heterojunction. Heteroatoms were introduced into the COFs linkage bonds through a post-synthesis modification scheme. The as-designed hybrid materials **Pd NPs@TTT-COF** exhibited remarkable photocatalytic activities as well as high stability and recyclability in a series of C–C cross-coupling reactions (Suzuki–Miyaura, Stille, Heck and Sonogashira) (Scheme 1).

Results and discussion

Imine-linked **TTI-COF** was converted to benzothiazole-linked **TTT-COF** by a post-synthetic sulfuration strategy,[7] Pd NPs were introduced to the **TTT-COF** substrates subsequently *via* an impregnation-reduction method to obtain **Pd NPs@TTT-COF**. The content of Pd in the composite material is 6.01 wt% determined by inductively coupled plasma mass spectrometry (ICP-MS).

As shown in Fig. 1a and b, the powder X-ray diffraction (PXRD) patterns exhibited six distinct diffraction peaks at 4.08°, 6.88°, 8.16°, 10.62°, 14.54° and 25.64° for **TTI-COF** and 4.16°,7.14°, 8.32°, 10.96°, 14.44° and 25.82° for **TTT-COF**, corresponding to the crystal planes of (100), (110), (200), (210), (310) and (001). The structure models of **TTI-COF** and **TTT-COF** were simulated by Material Studio (v. 7.0), and the experimental patterns of both showed good agreement with the each simulated PXRD pattern of eclipsed AA stacking models. (Fig. S1†) After Pawley refinement of experimental PXRD patterns, a unit cell with parameters $a = b = 25.54$ Å, $c = 3.51$ Å, $\alpha = \beta = 90°$, $\gamma = 120°$ and agreement factors $R_{wp} = 6.42\%$, $R_p = 4.67\%$ for **TTI-COF** and $a = b = 24.88$ Å, $c = 3.51$ Å, $\alpha = \beta = 90°$, $\gamma = 120°$ with $R_{wp} = 3.87\%$ and $R_p = 2.68\%$ for **TTT-COF** was obtained. An ordered sliding of the PXRD patterns was observed after sulfuration (Fig. 1c), which could be explained by the decrease of cell parameters (25.54 Å *vs.* 24.88 Å) from **TTI-COF** to **TTT-COF** according to Bragg's law. An almost undifferentiated PXRD pattern for **Pd NPs@TTT-COF** confirmed the retention of the crystal structure of **TTT-COF** after reduction by $NaBH_4$ and loading of Pd NPs (Fig. S2†).

The chemical transformation of **TTI-COF** to **TTT-COF** was verified by solid-state ^{13}C cross-polarization magic angle spinning nuclear magnetic resonance (CP-MAS NMR) spectroscopy and Fourier transform infrared (FT-IR) spectroscopy. As shown in Fig. 1d, the imine carbon 2 signal at 158 ppm was shifted to 169 ppm corresponding to thiazole carbon 2′ signal and merged into one peak with triazine carbon 1′ signal. Carbon 3 signal at 151 ppm was shifted to 3′ signal at 158 ppm and carbon 4 signal at 115 ppm disappeared due to integration of 4′ signal into the benzene rings range of 120–140 ppm. All these variations confirmed the formation of thiazole structures. A weak 151 ppm signal indicated trace amounts of unreacted imine structures. In the FT-IR spectra (Fig. 1f), the disappearance of the characteristic vibration of imine HC=N at 1625 cm^{-1} in **TTI-COF** and the presence of C=N vibration at 1608 cm^{-1} corresponding to thiazole units in **TTT-COF** confirmed successful conversion of **TTI-COF** to **TTT-COF**.[13] All characteristic peaks in **TTT-COF** were preserved in **Pd NPs@TTT-COF**, which manifested the retention of chemical structure after treatment.

The thermogravimetric analysis (TGA) curves (Fig. S3†) showed that benzothiazole-linked **TTT-COF** exhibited better thermal stability in comparison to imine-linked **TTI-COF**. Additionally, the chemical stability was significantly enhanced by the transformation of linkage. Both **TTI-COF** and **TTT-COF** can resist neutral and strong acidic (10 M HCl) conditions, however, structural collapses of **TTI-COF** were observed under strongly alkaline (10 M NaOH) and strongly reductive ($NaBH_4$) conditions whereas **TTT-COF** exhibited high tolerance to such extreme conditions (Fig. 2a and b). Considering that the reduction process *via* $NaBH_4$ was essential to prepare **Pd NPs@TTT-COF** and alkaline conditions were generally used in cross-coupling reactions, it is of great significance to improve the chemical stability of the substrates by locking the reversible imine linkage.

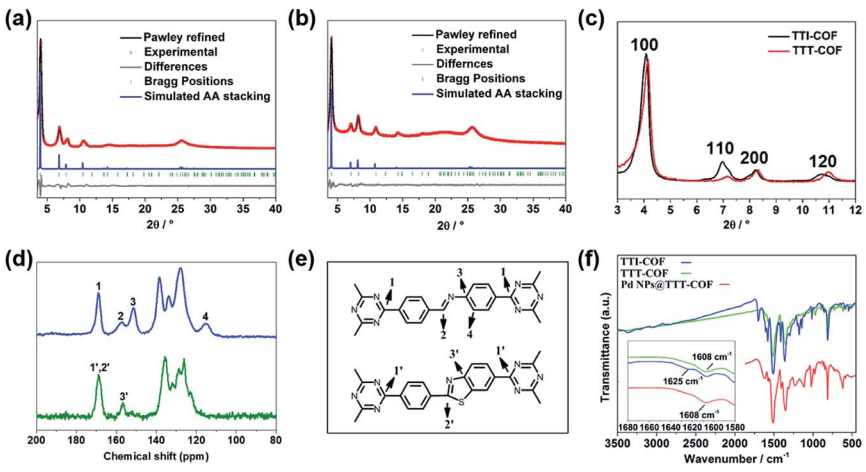

Fig. 1 Comparison of the experimental PXRD patterns of TTI-COF (a) and TTT-COF (b) with the Pawley refined pattern (black), simulated pattern for AA stacking (blue) and difference plot (green). Comparison of PXRD (c) and ^{13}C NMR (d) patterns between TTI-COF and TTT-COF. (e) Assignment of the ^{13}C signals to the respective ^{13}C nuclei in the structures. (f) Comparison of IR patterns between TTI-COF, TTT-COF and Pd NPs@TTT-COF.

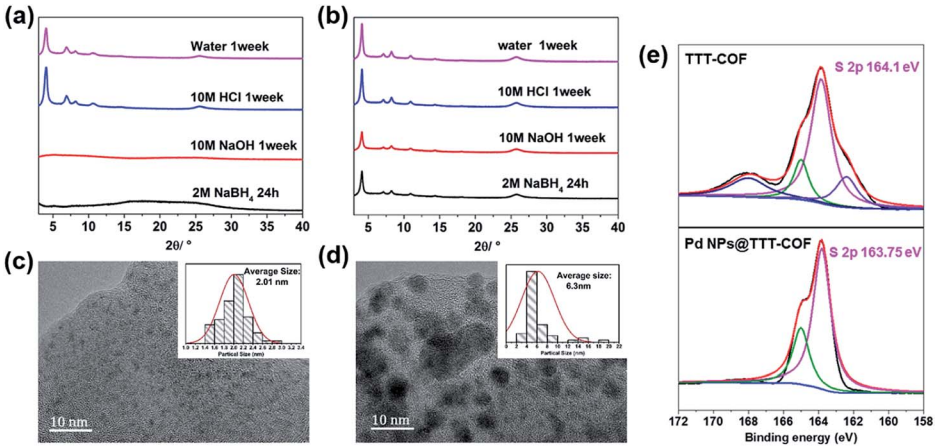

Fig. 2 PXRD patterns of TTI-COF (a) and TTT-COF (b) after processing under relevant conditions. HR-TEM images of **Pd NPs@TTT-COF** (c) and **Pd NPs@TTI-COF** (d), the insets are the size distribution profiles of Pd NPs. (e) S 2p region in the XPS spectra of TTT-COF before and after Pd loading.

The permanent porosities of COFs were assessed by measuring nitrogen adsorption isotherms at 77 K. All of **TTI-COF**, **TTT-COF** and **Pd NPs@TTT-COF** showed typical type-IV isotherms, which are characteristic of mesoporous materials. The Brunauer–Emmett–Teller (BET) surface areas of **TTI-COF**, **TTT-COF** and **Pd NPs@TTT-COF** were found to be 1659, 1640 and 1025 $m^2 g^{-1}$, with total pore volumes of 0.7024, 0.6989, and 0.434 $cm^3 g^{-1}$, respectively (Fig. S4†). The similar BET surface areas of **TTI-COF** and **TTT-COF** indicated that sulfuration process did not significantly change the porous structure, and an evident decrease of that in **Pd NPs@TTT-COF** confirmed that Pd NPs were distributed in pores within COFs. Pore size distribution (PSD) of **TTI-COF** and **TTT-COF** were derived from NLDFT as 2.34 and 2.16 nm, respectively, which were consistent with the reduction of cell parameters after sulfuration deduced by PXRD.

Scanning Electron Microscopy (SEM) was used to characterize the morphology of COFs. The characteristic petal-like morphology of **TTI-COF** formed by π–π stacking of the COF layers was maintained in **Pd NPs@TTT-COF** after sulfuration under high temperature, reduction by $NaBH_4$ and loading of Pd NPs (Fig. S5†). SEM-EDX elemental mapping exhibited homogeneous distribution of sulfur and palladium in COF substrate (Fig. S6†). Long-ordered channels of **TTT-COF** can be clearly observed in the high resolution transmission electron microscope (HR-TEM) image (Fig. S7†). The characteristic *d*-spacing of π–π stacking, which is equal to the distance between face-to face 2D TTO-COF plane. Another *d*-spacing of 2.16 nm is observed in the vertical direction. The *d*-spacing of 0.34 and 2.16 nm are corresponding to the diffraction peaks of (001) and (100) facets in the PXRD pattern according to Bragg's law ($n\lambda = 2d \sin\theta$). In the Fig. 2c, Pd NPs were distributed in **TTT-COF** substrate uniformly with an average particle size of 2.01 nm. The interplanar spacing of 0.23 nm in the region of Pd NPs corresponded to Pd (111) crystal plane (Fig. S7†). However, a larger and uneven size of Pd NPs (average size: 6.3 nm) was observed in **Pd NPs@TTI-COF** (Fig. 2d), which was similar to Au NPs and Pd NPs supported by TpPa-1 previously reported.[14,15] In addition, Pd NPs in **Pd NPs@TTI-COF** exhibited higher contrast and clearer lattice fringes in HR-TEM images than those in **Pd NPs@TTT-COF**, revealing that Pd NPs tend to be distributed on the surface of the **TTI-COF** substrate, whereas in **Pd NPs@TTT-COF**, more Pd NPs were encapsulated in the pores and interlayer of **TTT-COF**. This could be attributed to the addition of sulfur element. Sulfur atoms in benzothiazole groups could boost the anchoring effect of COFs substrates on Pd NPs and confine them in the internal pores of COFs to restrict their aggregation, thus Pd NPs can be distributed in the substrates with a finer and more uniform size.

X-ray photoelectron spectroscopy (XPS) was used to investigate the oxidation state of the Pd NPs and interactions between Pd species and COFs substrates. In the XPS spectra of **Pd NPs@TTT-COF**, the characteristic peaks of Pd $3d_{5/2}$ and $3d_{3/2}$ were located at 335.9 eV and 341.2 eV respectively (Fig. S8†), which were slightly higher than the binding energy (BE) values of metallic Pd (335.0 eV for Pd $3d_{5/2}$ and 340.3 eV for Pd $3d_{3/2}$) but much lower than the BE values of Pd(II) species, confirming that Pd(II) precursor was successfully reduced to Pd(0) by $NaBH_4$. The BE center of S 2p in **Pd NPs@TTT-COF** was located at 163.75 eV, exhibiting a negative shift of 0.3 eV compared with that in **TTT-COF**. Such positive and negative shift of BE for Pd 3d and S 2p were probably caused by the charge transfer from Pd NPs to S atoms, which confirmed the metal–ligands interactions between Pd NPs and S atoms of **TTT-COF** substrates.[16] The S 2p XPS spectra of **TTT-COF** exhibited two extra peaks in 168.3 and 162.8 eV, which is caused by the residual sulfur in **TTT-COF** after the sulfuration reactions. However, no changes were observed in BE of N 1s after Pd NPs loading in **TTT-COF**. These results revealed that sulfur atoms have a stronger interaction with Pd NPs than N atoms (Fig. S9†), which is an important factor for finer particle size of the Pd NPs in benzothiazole-linked **TTT-COF** than that in imine-linked **TTI-COF**.

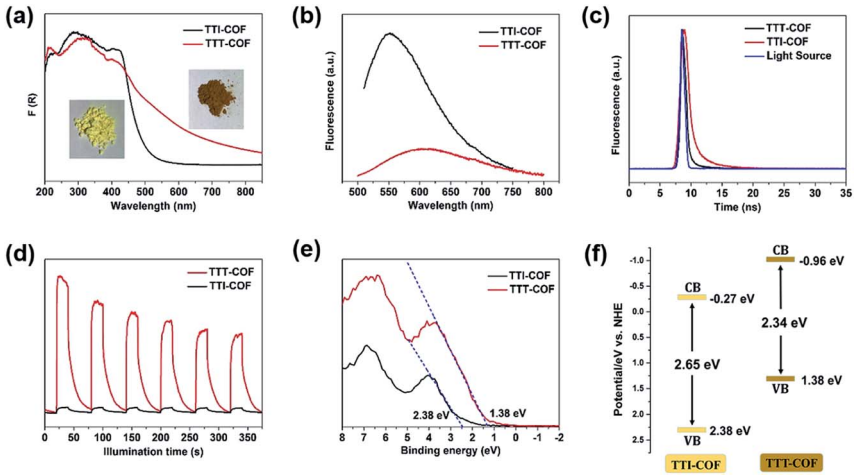

Fig. 3 (a) UV-DRS patterns of **TTI-COF** and **TTT-COF**, the insets are the photographs of the samples. (b) Steady-state photoluminescence (PL) spectra (b) and transient fluorescence spectra (c) of **TTI-COF** and **TTT-COF**. (d) Photocurrent measurements of **TTI-COF** and **TTT-COF**. (e) VB XPS spectra of **TTI-COF** and **TTT-COF**. (f) Band alignment of **TTI-COF** and **TTT-COF**.

In the UV-DRS spectrums, **TTT-COF** exhibited a broader absorption band in the visible region than **TTI-COF** (Fig. 3a) with a band narrowing of 0.3 eV (Fig. S10†), revealing that the sulfuration of COFs can improve the light-harvesting efficiency in the visible region and narrow the optical bandgap. Compared with **TTI-COF**, a significant decrease of fluorescence of **TTT-COF** meant lower recombination rate of photogenerated electron–hole pairs (Fig. 3b), and a shorter transient fluorescence lifetime of **TTT-COF** confirmed higher conduction efficiency of photocarriers[17,18] (Fig. 3c). In addition, higher photocurrent response of **TTT-COF** also indicated better separation and migration of photocarriers in COFs with benzothiazole linkages (Fig. 3d), which could be attribute to the enhanced π-conjugation within the COF planes from imine linkages to benzothiazole linkages. A similar result was also confirmed in previous report of benzoxazole-linked COFs.[5] The valence band X-ray photoelectron spectroscopy (VB XPS) was used to investigate the variation of band structure in **TTI-COF** after sulfuration. The VB edges of **TTI-COF** and **TTT-COF** were located at 2.38 and 1.38 eV (Fig. 3e), and the conduction band (CB) potential were calculated as −0.27 and −0.96 eV, respectively, according to the formula $E_{CB} = E_{VB} - E_g$.

Palladium catalysts have been widely used in C–C cross-coupling reactions, but the conditions of heating and reflux are necessary for most of these reactions. Considering that NPs with ultrafine size would generally exhibit better catalytic performance and **TTT-COF** is a photosensitive semiconductor, the Suzuki–Miyaura cross-coupling reaction of iodotoluene and phenylboronic acid under visible light was used as a model reaction to investigate the photocatalytic activity of **Pd NPs@TTT-COF**. The reaction system included iodotoluene (0.3 mmol), phenylboronic acid (0.4 mmol), excess potassium carbonate and 5 mg photocatalyst in ethanol/H_2O, an excellent yield (99%) of desired product biphenyl was obtained within an hour under visible light. The turnover frequency (TOF) of the composite photocatalyst for the model reaction was calculated as 344 h^{-1}, which is significantly higher than that of previous Pd NPs loaded photocatalysts (Table S3†). A series of control experiments were carried out (Table 1), which confirmed that illumination, Pd NPs and **TTT-COF** substrates were all necessary for this photocatalytic Suzuki–Miyaura reaction. Additionally, *p*-benzoquinone (BQ, an electron scavenger) and diisopropylethylamine (iPr_2NEt, a hole scavenger) were added to the reaction system respectively to investigate the mechanism of the photocatalytic reaction. The photocatalytic cross-coupling reaction was greatly blocked in the presence of BQ and iPr_2NEt, respectively. When both were added to the reaction system, the reaction was almost blocked. It can be seen that photogenerated electrons and holes were both significant to the photocatalytic Suzuki–Miyaura cross-coupling reaction.

In the light of the above results and relevant studies,[19] we proposed a possible reaction mechanism of this photocatalytic Suzuki–Miyaura reaction as shown in Scheme 2. Upon the

Table 1 Control experiments for the model reaction

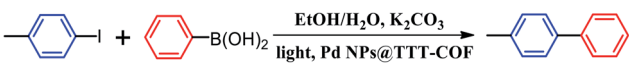

Entry	Photocatalyst	Light	Additive[b]	Yield[c]/%
1	**Pd NPs@TTT-COF**[a]	✓		99
2	**TTT-COF**	✓		N.D.
3	-	✓		N.D.
4	**Pd NPs@TTT-COF**	✗		22
5	**Pd NPs@TTT-COF**	✓	BQ	31
6	**Pd NPs@TTT-COF**	✓	iPr_2NEt	37
7	**Pd NPs@TTT-COF**	✓	BQ + iPr_2NEt	Trace

[a] Reaction conditions: 4-iodotoluene (0.3 mmol), phenylboronic acid (0.35 mmol), K_2CO_3 (0.6 mmol), 6 mL ethanol/H_2O, Xe lamp (>420 nm), room temperature, N_2 atmosphere. [b] The amount of additives was 1 mmol. [c] Yields were determined by GC-MS.

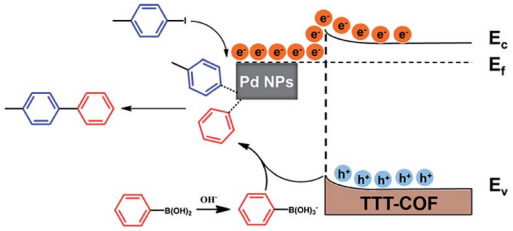

Scheme 2 Proposed mechanism for the photocatalytic model.

irradiation of visible light, electrons on the VB of **TTT-COF** were excited to jump to the CB and migrate to Pd NPs which act as electron sink. C–I bonds of the adsorbed iodotoluene will become longer when excited electrons on the surface of the electron-rich Pd NPs enter the unoccupied orbital of iodotoluene, which facilitated the cleavage of the C–I bond to generate phenyl radicals and forming the intermediate of organometallic complex. The $B(OH)_2$ groups of phenylboronic acid were converted into $B(OH)_3^-$ groups under the alkaline atmosphere, and the C–B bonds were cleaved by photogenerated holes to generate another phenyl radical. After the process of reductive elimination, the desired product biphenyl was generated and Pd catalysts were regenerated.

Pd NPs@TTT-COF exhibited superior stability and reusability. Almost no loss of activity was found in the model reaction among the four recyclings of photocatalyst (Fig. S11†). No significant changes were observed in the PXRD and IR patterns of **Pd NPs@TTT-COF** before and after the fourth run of the photocatalytic reaction (Fig. S12†) which benefited from the good chemical stability of benzothiazole-linked **TTT-COF**. Moreover, the porosity of **Pd NPs@TTT-COF** was also well maintained after four cycles, the BET surface areas was found to be 1003.2 $cm^3\ g^{-1}$. As shown in the TEM images, there is no significant increase in the size of Pd NPs after the fourth run, (Fig. S13†) whereas in previous reports of metal NPs@TpPa-1, the size of NPs was increased with the number of cycles.[14] The loading rate of Pd in the composite photocatalyst (5.88 wt%) dropped slightly after four cycles determined by ICP-MS. These results can be attributed to the high chemical stability of **TTT-COF** and the strong anchoring effect of the benzothiazole groups in **TTT-COF** to Pd NPs.

The photocatalytic performance of **Pd NPs@TTT-COF** in photocatalytic C–C cross-coupling reactions was further investigated (Table 2). Satisfactory conversions (82–99%) of various substrates were observed in the photocatalytic Suzuki–Miyaura reactions. Iodobenzenes with electron-donating substituents showed lower conversions compared to the electron-withdrawing ones, which can be explained by the fact that the electron-rich aryl iodides are not easily attacked by the electrons on the Pd NPs to result in the cleavage of C–I bond. On the contrary, phenylboronic acid with electron-withdrawing substituents exhibited lower conversion because electron-deficient phenylboronic acids were not favorable to react with positive holes (h^+). In addition, *meta*-methyl substituted iodobenzene and phenylboronic acid showed lower conversions which could be attribute to electronic effect and steric

Table 2 **Pd NPs@TTT-COF** photocatalyzed C–C cross-coupling reactions with different aryl iodides. Values in parentheses are the TOF values (h^{-1}).

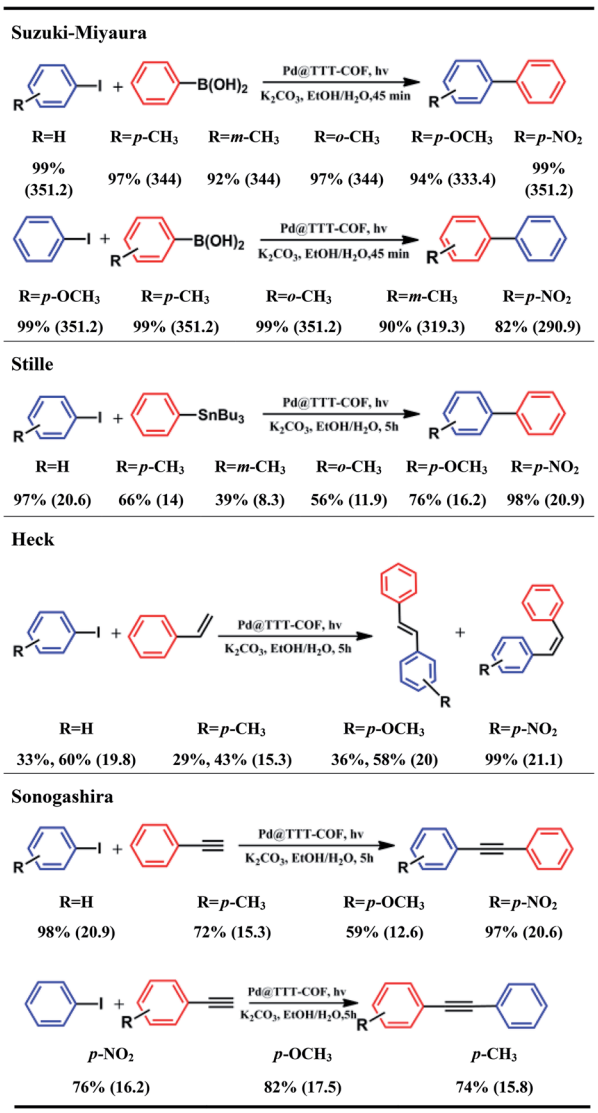

hindrance.[20] Surprisingly, **Pd NPs@TTT-COF** has also shown excellent efficiency of photocatalysis in a series of other classic C–C cross-coupling reactions (Stille, Heck and Sonogashira). The reactants with electron-withdrawing substituents still exhibited higher conversions in such reactions, suggesting that the series of C–C cross-coupling reactions could probably follow similar reaction mechanisms. The TOF of each reaction was calculated to be higher than that of other reported photocatalysts, (Table S3†) which was mainly attributed to two factors: (1) the ultrafine size and uniform distribution of Pd NPs resulted in higher contact area and more catalytic sites of Pd catalysts; (2) benzothiazole-linked π-conjugated COFs frameworks exhibited a strong photoelectric response, indicating high photoelectron density on Pd NPs and the increased the catalytic efficiency. Interestingly, it is noted that *cis*-stilbene

accounted for a large part of the products of the photocatalytic Heck reactions whereas *trans*-stilbene was the main product in previous reports.[15] Control experiments have been carried out to prove that isomerization of stilbene from trans (*E*) form to cis (*Z*) form can be catalyzed by **Pd NPs@TTT-COF** under the visible light irradiation (Table S4†). Recently, Banerjee's group reported a triazine functionalized COF (TpTt) for the *E* to *Z* isomerization of *trans*-stilbene *via* a process of triplet state excitation,[21] and triazine groups have also been found to play an important role in the photoisomerization of stilbene.[22] Hereby, we believed that the cis products of the photocatalytic Heck reactions were obtained by photoisomerization of the original trans products catalyzed by triazine-based **TTT-COF** substrate *via* a similar mechanism.

Conclusions

In summary, we have developed a hybrid material **Pd NPs@TTT-COF** photocatalyst. Several advantages of benzothiazole-linked COFs substrate were proved as follows: (1) superior chemical stability makes the COFs substrate resistant to extreme conditions in the preparation and application of catalysts; (2) benzothiazole-linked conjugated framework exhibited higher conduction efficieney of photocarriers; (3) Pd NPs were anchored by S atoms of benzothiazole groups in the pores of COFs with an ultrafine and uniform particle size. **Pd NPs@TTT-COF** showed superior photocatalytic performance and reusability in a series of C–C cross-coupling reactions. Considering the designability of COFs as well as the diversity of metal NPs, this strategy will provide great opportunities for the design and synthesis of photocatalysts for a wide range of applications. This work would inspire researchers that the linkage could also bring some fascinating properties to COFs.

Conflicts of interest

There are no conflicts to declare.

Acknowledgements

This work was supported by the National Key Research and Development Program (2016YFA0203100), the National Natural Science Foundation of China (21537004, 21621064, 21777169).

References

1 S. Y. Ding and W. Wang, *Chem. Soc. Rev.*, 2013, **42**, 548.
2 X. Feng, X. Ding and D. Jiang, *Chem. Soc. Rev.*, 2012, **41**, 6010.
3 C. S. Diercks and O. M. Yaghi, *Science*, 2017, 355.
4 E. Jin, M. Asada, Q. Xu, S. Dalapati, M. A. Addicoat, M. A. Brady, H. Xu, T. Nakamura, T. Heine, Q. Chen and D. Jiang, *Science*, 2017, **357**, 673.
5 P. F. Wei, M. Z. Qi, Z. P. Wang, S. Y. Ding, W. Yu, Q. Liu, L. K. Wang, H. Z. Wang, W. K. An and W. Wang, *J. Am. Chem. Soc.*, 2018, **140**, 4623.
6 P. Das and S. K. Mandal, *Chem. Mater.*, 2019, **31**, 1584.
7 F. Haase, E. Troschke, G. Savasci, T. Banerjee, V. Duppel, S. Dorfler, M. M. J. Grundei, A. M. Burow, C. Ochsenfeld, S. Kaskel and B. V. Lotsch, *Nat. Commun.*, 2018, **9**, 2600.
8 P. J. Waller, S. J. Lyle, T. M. Osborn Popp, C. S. Diercks, J. A. Reimer and O. M. Yaghi, *J. Am. Chem. Soc.*, 2016, **138**, 15519.
9 B. Zhang, M. Wei, H. Mao, X. Pei, S. A. Alshmimri, J. A. Reimer and O. M. Yaghi, *J. Am. Chem. Soc.*, 2018, **140**, 12715.
10 Q. Gu, Q. Jia, J. Long and Z. Gao, *ChemCatChem*, 2019, **11**, 669–683.
11 S. Lu, Y. Hu, S. Wan, R. McCaffrey, Y. Jin, H. Gu and W. Zhang, *J. Am. Chem. Soc.*, 2017, **139**, 17082.
12 R. Tao, X. Shen, Y. Hu, K. Kang, Y. Zheng, S. Luo, S. Yang, W. Li, S. Lu, Y. Jin, L. Qiu and W. Zhang, *Small*, 2020, 1906005.
13 M. G. Rabbani, T. Islamoglu and H. M. El-Kaderi, *J. Mater. Chem. A*, 2017, **5**, 258.
14 P. Pachfule, S. Kandambeth, D. D. Diaz and R. Banerjee, *Chem. Commun.*, 2014, **50**, 3169.
15 P. Pachfule, M. K. Panda, S. Kandambeth, S. M. Shivaprasad, D. Diaz Diaz and R. Banerjee, *J. Mater. Chem. A*, 2014, **2**, 7944.
16 H. I. Lee, S. H. Joo, J. H. Kim, D. J. You, J. M. Kim, J.-N. Park, H. Chang and C. Pak, *J. Mater. Chem.*, 2009, **19**, 5934.
17 Q. Jia, S. Zhang and Q. Gu, *J. Energy Chem.*, 2019, **30**, 152–161.
18 Q. Jia, S. Zhang, X. Jia, X. Dong, Z. Gao and Q. Gu, *Catal. Sci. Technol.*, 2019, **9**, 5077–5089.
19 Z. J. Wang, S. Ghasimi, K. Landfester and K. A. I. Zhang, *Chem. Mater.*, 2015, **27**, 1921.
20 D. Sun and Z. Li, *J. Phys. Chem. C*, 2016, **120**, 19744–19750.
21 M. Bhadra, S. Kandambeth, M. K. Sahoo, M. Addicoat, E. Balaraman and R. Banerjee, *J. Am. Chem. Soc.*, 2019, **141**, 6152.
22 K. Ohara, Y. Inokuma and M. Fujita, *Angew. Chem., Int. Ed.*, 2010, **49**, 5507.